# Consequences of the additional presence of MC carbides on the behavior in oxidation at 1000°C of a cast Cantor high entropy alloy”

Patrice Berthod

## To cite this version:

Patrice Berthod. Consequences of the additional presence of MC carbides on the behavior in oxidation at 1000°C of a cast Cantor high entropy alloy”. Materials and Corrosion / Werkstoffe und Korrosion, 2023, 74 (9), pp.1312-1323. ⟨10.1002/maco.202213721⟩. ⟨hal-04768582⟩

HAL Id: hal-04768582

https://hal.science/hal-04768582v1

Submitted on 6 Nov 2024

# “Consequences of the additional presence of MC carbides on the behavior in oxidation at 1000°C of a cast Cantor high entropy alloy”

Patrice Berthod

**Materials and Corrosion – Werkstoffe und Korrosion, 2023, 74(9), 1312–1323.**

# Consequences of the additional presence of MC carbides on the behavior in oxidation at 1000°C of a cast Cantor high entropy alloy

Patrice Berthod[1,2,*]
[1]Université de Lorraine, Faculté des Sciences et Technologies, F-54500 Vandoeuvre-lès-Nancy, France
[2]CNRS, IJL, F-54000 Nancy, France
*Corresponding author's e-mail address: patrice.berthod@univ-lorraine.fr

**Abstract.** MC carbides can be successfully obtained in grain boundaries of some HEA alloys of the Cantor type, to improve significantly their mechanical properties at high temperature. They can be also not neutral for the oxidation behavior. To explore their possible influence in this field, an equimolar CoNiFeMnCr reference alloy and two versions containing TaC or HfC carbides were prepared by casting and exposed to air at 1000°C. Their oxidation behaviors were studied by characterizing the obtained corrosion products and the modifications induced in the subsurfaces of the samples. Results show that TaC and HfC are moderately involved in the oxidation phenomena but they obviously influence the Cr and Mn diffusion toward the oxidation front. This seemingly aggravates more the already poor oxidation high temperature resistance of the base alloy. However the harmful effect of the TaC seems to be much lower than the one of the HfC, and the TaC–strengthened CoNiFeMnCr alloy is only a little less resistant against oxidation than the carbide–free reference equimolar alloy.

**Keywords :** Cantor alloy ; CoNiFeMnCr equimolar ; TaC; HfC; High temperature oxidation

The Author states that:

**Data availability statement**: no data is available

**Funding statement:** this work did not benefit from any funding for this research

**Conflict of interest disclosure:** there is no conflict of interest associated to this work

**Ethics approval statement:** he approves the ethics

**Patient consent statement:** not applicable

**Permission to reproduce material from other sources:** not applicable

**Clinical trial registration:** not applicable

## Introduction

The needs of high performance coarse–grained metallic materials, for fabricating complex–shaped components working at high temperature, stay important despite the progress of additive manufacturing. For achieving mechanical properties high enough at temperatures close to 1000°C and sometimes beyond, great grain size and dendritic coarseness are to be preferred. This is one of the reasons of the presence of Single–Crystalline (SX) or Directionally Solidified (DS) superalloys in the hottest zones of turbines (e.g. static and mobile blades) or glass–making (e.g. spinners) processes. The potential weak points of polycrystalline SD or equiaxed alloys are the grain boundaries (GB) and the interdendritic spaces (IS), from that the presence of strengthening phases in these areas. Among these particles allowing the reinforcement of GB and IS there are carbides. These ones can be of various types but, among the most efficient ones in this role, there are monocarbides formed by involving selected carbide–forming elements as Ta or Nb, and even Hf and Zr. All these metals [1] are able to form an interdendritic and intergranular network of MC carbides which enhance the high temperature mechanical properties, static tensile strength and creep resistance [2–4]. To push further the high temperature mechanical resistance working on the matrix is complementary. Indeed, matrix is generally the main From several decades this classically done by solid solution strengthening (substitutional heavy atoms dispersed in solid solution) or by hard particles precipitation (secondary carbides, intermetallic precipitates, dispersoids). One can also imagine to apply the base principle of the High Entropy Alloys (HEA) [5] to the austenitic matrixes of cast polycrystalline MC–reinforced superalloys, by replacing the Ni(Al) or Co(Cr) austenitic solid solutions by a mix, in similar proportions, of several metals chosen among Co, Cr, Cu, Fe, Mn, Ni … Despite HEAs exist since already several decades ago [6], this seems to do not have been tested until very recently. If this is really the case, the alloys resulting from the association of the well–known equimolar CoNiFeMnCr composition [7–10] with primary TaC or HfC, elaborated and microstructurally characterized [11,12] are possibly the first specimens of this family to have been considered. The Co–Ni–Fe–Mn–Cr system was among the early first HEAs to be studied and extensive investigations were carried out concerning them, in the fields of thermodynamic [13], magnetic [14], diffusion behavior [15] or strengthening [16,17]. This alloy was logically chosen to test, in a first time if this was possible to obtain TaC or HfC carbides similar to the ones strengthening cobalt–based or nickel–based alloys efficiently [2,3], and in a second time to check whether the presence of these carbides really brought significant reinforcement to equimolar CoNiFeMnCr alloy. These tests confirmed that script–like eutectic TaC [11] or HfC [12] carbides were successfully obtained in the spaces separating grains and the ones separating the dendrites of matrix from one another, and that the creep resistance at high temperature was really enhanced by their presence [18].

One of the other most important properties for alloys developed for applications inducing elevated working temperatures is the resistance against oxidation. Equimolar CoNiFeMnCr alloys containing TaC or HfC may present potential problems in this field, for several reasons. First, the equimolar principle automatically limits the Cr content to around 20 wt.%, which is in the bottom side of the Cr content range usually respected for chromia–forming high temperature alloys or superalloys. Second, particles rich in Ta or Hf (which are highly oxidable metals), furthermore located in the grain and interdendritic boundaries (which are zones known to be high diffusion pathways for the species involved in the oxidation phenomena), may degrade the oxidation behavior.

A series of investigations were already carried about the behavior of HEAs in high temperature oxidation. Among the studied alloys which are the closest to the Cantor composition but which are slightly different, there are Mn–free Al–containing ones (AlCoCrFeNi) [19,20], or some Ni–free ones [21,22], for instance. The oxidation behavior of the equimolar CoNiFeMnCr composition was specifically investigated in laboratory air at temperatures from 500°C to 900°C [23,24], and in synthetic air between 900 and 1100°C [25]. In this later study, it was notably observed that Cr and Mn had the most important roles in the oxidation process; after 24 hours of oxidation they were particularly present in the external and internal corrosion products ($Mn_3O_4$, $(Mn,Cr)_3O_4$ and $Cr_2O_3$.

The purpose of this work is to explore the oxidation behavior of the matrix and of the whole alloys in air at 1000°C during 50 hours, and compare them to alloys containing only a single base element (Ni, or Co, or Fe). These investigations concern then: an equimolar CoNiFeMnCr alloy (named “CTR alloy”) with comparison with Co(Cr) and Ni(Cr) alloys, and a CTR alloy added with TaC, and another one added with HfC, with comparison with Co(Cr)+TaC or HfC, Ni(Cr)+HfC and Fe(Cr)+HfC at similar temperatures.

## Materials and methods

Three alloys were elaborated by melting and solidification in inert atmosphere. The three compositions of interest, selected among the five ones recently studied concerning their as–cast microstructures [11,12], are: the equimolar CoNiFeMnCr (about 40g), the same with Ta and C additions to reach 0.25 wt.% C and 3.7wt.% Ta in the whole second alloy (named “CTR+TaC”), and the same with Hf and C additions to reach 0.25 wt.% C and 3.7wt.% Ta in the whole third alloy (“CTR+HfC”). After accurate weighing (balance with a 0.1 mg precision), and mixing pure elements (Alfa Aesar, purity > 99.9%) in the water–cooled copper crucible of the furnace, the melting chamber was closed by placing – between the copper crucible (inside) and the induction coil (outside) – a silica tube. The laboratory air was replaced by an inert atmosphere composed of pure argon at the 300 mbars internal pressure. Heating, melting, chemical homogenization in the liquid state (during ten minutes) were achieved by creating, in the water–cooled copper coil, a 100 kHz alternative current (maximal voltage: 5 kV). To allow solidification and solid state cooling, the applied voltage was progressively decreased down to zero.

The three obtained ingots, not easily machinable due to their ovoid shape, were embedded in resin to be cut with a metallographic saw. Per alloy, two parts were obtained, one for the as–cast microstructure and chemical composition controls, and one for the oxidation test. The first type of sample was simply re–embedded in resin to be ground (SiC papers from #240 to #1200) and polished (textile disk periodically re–enriched in hard micrometric particles by spraying). At the end the obtained mirror–like samples were ready to control their microstructure by Scanning Electron Microscopy (SEM JEOL JSM6010LA) in Back Scattered Electrons mode (BSE), and their chemical composition by Energy Dispersion Spectrometry (EDS). The second type of sample, of a parallelepipedic shape (dimensions: 3 mm × 10 mm × 10 mm approximately), was ground with #1200 SiC papers on its six faces. Edges and corners were additionally smoothed using the same SiC papers.

The three samples of the second type were placed on a ceramic platform which was introduced in the hottest zone of a resistive furnace at 1000°C, where they stayed during 50 hours. At the end of this isothermal stage, the furnace was switched off and the samples cooled in the still closed furnace. When the internal temperature was the ambient one, the furnace was opened and the oxidized samples carefully exited and handled. Characterization started by X-Ray Diffraction performed on the oxidized surfaces (XRD, Bruker D8 Advance, copper Kalpha radiation). Samples were thereafter embedded in resin, cut in order to obtain cross–sectional metallographic samples to grind and polish. The aged and oxidized states of the mirror–like samples were characterized using the same techniques and apparatus as described above (SEM, EDS).

## Results and discussion

### *Control of the as–cast states*

The microstructures of the three alloys are illustrated by the SEM/BSE micrographs presented in Figure 1. The CTR alloy is single–phased and the two other alloys are double–phased. The “CTR+TaC” alloy contains mainly finely structured eutectic TaC alloys and, in minority, coarser TaC. The carbides present in the “CTR+HfC” alloy are also of two types, the principal one being eutectic HfC and the other one HfC a little coarser than the first cited. The chemical compositions analyzed by EDS full frame analysis (five □250 areas) well fit the targeted one (Table 1).

EDS did not allow controlling the carbon content in these full frame areas but EDS spot analysis was possible on the coarsest carbides found in the microstructures. TaC and HfC were thus identified and their surface fractions were in good agreement with the targeted C contents which were thus considered as well respected too.

### *Oxidation state of the equimolar CoNiMnCr alloy (CTR)*

XRD led to the diffractogram presented in Figure 2. It was observed at the end of the oxidation test that many parts of oxides were lost during cooling. Oxide spallation led to parts of surface to be exposed to X–rays with as results some peaks corresponding to the austenitic alloy (FCC). The other peaks were indexed as corresponding to the $Cr_2O_3$, $Mn_2O_3$, $Mn_3O_4$, $MnCr_2O_4$ and MnO. The SEM/BSE pictures presented in Figure 3 give a general view of the oxidized surface state and a magnified view of a zone where a maximum of external oxide was kept. Obviously, the thickness of oxide can be divided in two parts. The inner oxide layer, rather compact and which seems having grown inwards (irregular front of oxidation penetration), was generally kept all around the sample. The outer oxide scale, much more porous, was lost here and there during cooling. When observed at high magnification (Figure 4) the oxides appear with different gray levels. EDS spot analysis allowed identifying $M_3O_4$–type oxides (M being Mn and Cr in various relative proportions), some of them being very close to the spinel $MnCr_2O_4$. Some isolated chromia oxides ($Cr_2O_3$) were also noticed, principally at the interface between the oxide scale and the alloy. The natures of the obtained oxides (XRD, EDS) are in good agreement with what was earlier observed concerning the oxidation of equimolar CoNiFeMnCr alloys at temperature equal or close to 1000°C for a little shorter durations (12h or 24h) [21, 24]. The presence of porosities in the subsurface can be attributed to the Kirkendall pores formation induced by oxidation. This Kirkendall phenomenon, the tendency to oxide spallation, were previously noticed for induction cast equimolar CoNiFeMnCr alloys oxidized at 1000°C [24].

### *Oxidation state of the CTR+TaC alloy*

A part of the oxides formed on the surface of the CTR+TaC alloy during the stage at 1000°C also spalled off during cooling. The alloy was detected by XRD and the oxides identified thanks to the obtained peaks were globally the same as for the carbide–free equimolar alloy, except the additional presence of a tantalum oxide $Ta_2O_5$ (Figure 5). The $CrTaO_4$ mixed oxide, which may result from the reaction between $Ta_2O_5$ with $Cr_2O_3$, is also present, obviously. The SEM/BSE micrographs presented in Figure 6 and Figure 7 show that the oxide scale was, here too, composed of an outer part, in majority lost by spallation during cooling (some isolated parts stayed, fortunately), and of an inner one (grown inwards) which was better kept by the alloy. As observed for the CTR alloy, the oxides rich in Cr are mainly in contact with the alloy while the ones rich in Mn tend to be farer the scale/alloy interface. The oxides involving tantalum are concentrated at this interface for some of them. Other $CrTaO_4$ formed in the subsurface. Kirkendall pores are present in an about 50 µm depth form the scale/alloy interface, where another alloy modification also occurred: the disappearance of the tantalum carbides (over a 30–40 µm depth). One can see, in addition, that secondary fine TaC carbides precipitated in the matrix, deeper than this zone (and in the bulk too). Even if this is not the purpose of this study one can say that this rather fine, dense and homogeneous presence of secondary TaC allows identifying the {1000°C, 50 hours} conditions as being an efficient precipitation treatment potentially producing additional creep resistance for the alloy.

### *Oxidation state of the CTR+HfC alloy*

XRD was also run on the oxidized surface of the CTR+HfC alloy prior to the cross–section preparation (Figure 8). As observed for the CTR+TaC alloy, the detected oxides are the same as for the reference CTR alloy. A new oxide needs to be added to the list: $HfO_2$. Seemingly the CTR+HfC alloy was more severely deteriorated by oxidation than the two former alloys, with notably a particularly deep internal oxidation (Figure 9). The principal scale was again composed of an outer part (partly lost by spallation during cooling) and an inner part with an irregular frontier with alloy, along which the oxides are richer in Cr (chromia parts were notably found). The hafnium carbides were oxidized, even the coarse pre–eutectic ones for which the oxidation progression from periphery to the carbide center can be observed in the right–bottom corner of the right SEM/BSE image in Figure 10.

*Elemental distribution in the subsurface of the oxidized alloys*

The SEM/BSE and EDS characterization of the surfaces and sub-surfaces of the oxidized alloys were enriched by running X–maps acquisitions. Figure 11, Figure 12 and Figure 13 show some of the obtained X–maps for the CTR, CTR+TaC and CTR+HfC alloys, respectively. These qualitative but general chemical analyses allow seeing clearly, for instance, the double oxide layer composed of the inner Cr–rich one and the outer Mn–rich one. Another interesting observation concerns the subsurface impoverishment in Cr and in Mn, over several tens of micrometers from the interface with the oxide scale.

*Analysis of the {Cr and Mn}–depleted depths using EDS concentration profiles*

To estimate more accurately the losses in Cr and Mn of the alloys evidenced by the X–maps a series of concentration profile acquisitions were carried out in the subsurface of each alloy. Some of the obtained concentration profiles are presented in Figure 14. Obviously this was manganese which was the most lost during the oxidation of the alloys. For each alloy the Mn–depletion seems more extended than the Cr–depletion and the minimal content, obtained for both elements at the {oxide scale / alloy} interface, is much lower for Mn than for Cr. These observations are quantitatively confirmed by the results displayed in Table 2.

By analyzing these results it additionally appears that the minimal Cr and Mn contents in extreme alloy surface are lower for the carbides–containing alloys than for the carbide–free equimolar alloy (Mn: true for both alloys, Cr: true only for the CTR+HfC alloy). The Cr–depleted depths are almost the same for the three alloys but the Mn–depleted depths of the carbides–containing alloys are greater than for the carbide–free equimolar alloy. This can be due, either to an easier diffusion of Mn in presence of carbides in the interdendritic and intergranular boundaries, or to a faster oxidation involving Mn when carbides are present.

*Estimation of the masses and thickness of the oxides*

The profiles were exploited to deduce the masses of Cr and of Mn lost per surface unit area by the oxidizing alloys. The (1) and (2) formula were used:

$$\frac{m_{Cr}}{S} = \rho_{alloy} \times \int_0^{Ddepth_{Cr}} [f_W^{Cr} - f_W^{Cr}(x)] \times dx \qquad (1)$$

$$\frac{m_{Mn}}{S} = \rho_{alloy} \times \int_0^{Ddepth_{Mn}} [f_W^{Mn} - f_W^{Mn}(x)] \times dx \qquad (2)$$

Where $\frac{m_{Cr}}{S}$ and $\frac{m_{Mn}}{S}$ are respectively the Cr and Mn masses lost, per surface unit area, by the oxidizing alloy, $\rho_{alloy}$ is the volume mass of the alloy (estimated values: 7.9g cm$^{-3}$ for CTR, 8.1g cm$^{-3}$ for CTR+TaC, and 8.1g cm$^{-3}$ for CTR+HfC), $f_W^{Cr}$ and $f_W^{Mn}$ are the Cr and Mn weight contents in the initial alloy, $f_W^{Cr}(x)$ and $f_W^{Mn}(x)$ are the current Cr and Mn weight contents in the oxidized alloy at the depth $x$ in the subsurface and $Ddepth_{Cr}$ and $Ddepth_{Mn}$ are the Cr–depleted and Mn–depleted depths respectively.

Assuming that these quantities of Cr and of Mn were oxidized these first results may allow estimating the mass of the formed oxides. Despite that the natures of these ones were multiple, the metallographic results also showed that the $MnCr_2O_4$ and $(Mn,Cr)_3O_4$ species dominate. Further calculations were thus done on the basis of exclusive $(Mn,Cr)_3O_4$ formation, to simplify and for the feasibility of the determination. After having converted the masses per surface unit area into numbers of moles per surface unit area $\left(\frac{n_{Cr}}{S}\text{ and }\frac{n_{Mn}}{S}\right)$ using the molar masses of both elements ($M_{Cr}$ and $M_{Mn}$), according to the (3) and (4) equations, the numbers of oxygen moles and of $(Mn,Cr)_3O_4$ moles per surface unit area ($\frac{n_O}{S}$ and $\frac{n_{(Mn,Cr)_3O_4}}{S}$) were calculated using the (5) and (6) formula. The mass of $(Mn,Cr)_3O_4$ per surface unit area $\frac{m_{(Cr,Mn)_2O_3}}{S}$ was determined from the (7) formula. The oxide mass was finally deduced, according to the (8) formula, in which the value for the oxide density ($\rho_{(Mn,Cr)_3O_4}$) was taken equal to 4.86 g $cm^{-3}$.

$$\frac{n_{Cr}}{S} = \left[\frac{\frac{m_{Cr}}{S}}{M_{Cr}}\right] \quad (3) \qquad\qquad \frac{n_{Mn}}{S} = \left[\frac{\frac{m_{Mn}}{S}}{M_{Mn}}\right] \quad (4)$$

$$\frac{n_O}{S} = \frac{4}{3} \times \left(\frac{n_{Cr}}{S} + \frac{n_{Mn}}{S}\right) \quad (5) \qquad\qquad \frac{n_{(Mn,Cr)_3O_4}}{S} = \frac{1}{4} \times \frac{n_O}{S} \quad (6)$$

$$\frac{m_{(Cr,Mn)_2O_3}}{S} = \frac{n_{(Mn,Cr)_3O_4} \times (3 \times (M_{Cr} + M_{Mn}) / 2 + 4 \times M_O)}{S} \qquad (7)$$

$$e_{(Mn,Cr)_3O_4} = \frac{\frac{m_{(Mn,Cr)_3O_4}}{S}}{\rho_{(Mn,Cr)_3O_4}} \qquad (8)$$

Table 3 gathered the results obtained for the masses of Cr and Mn lost by the alloys during oxidation, and the corresponding values of the masses (per surface unit area) and equivalent thicknesses of the $(Mn,Cr)_3O_4$ scales. The 16 to 21 µm of $(Mn,Cr)_3O_4$ thickness for the CTR alloy are a rather lower than suggested by micrographs. This can be explained by the presence of many pores/voids in the thick outer part of the scale. The agreement is better for the CTR+TaC and CTR+HfC alloys.

*Corresponding mass gain kinetic values*

The total mass gains at the end of the 50 hours of oxidation at 1000°C were estimated by calculating, according to (9), the mass of oxygen gained by the alloys by surface unit area, using the numbers of moles of Cr, Mn and finally O resulting from the (3), (4) and (5) equations above. The parabolic constant Kp was thereafter estimated using equation (10):

$$\frac{m_O}{S} = \frac{n_O}{S} \times M_O \qquad (9)$$

$$Kp = \frac{1}{2} \times \frac{\left(\frac{m_O}{S}\right)^2}{50h} \qquad (10)$$

The obtained values are displayed in Table 4. The values obtained for the mass gain ("Gained O" column) for the three alloys together are spread out over the [2 $mg/cm^2$ – 7 $mg/cm^2$] range which is rather in good agreement with the 4.45 mg/cm$^2$ earlier found for another equimolar CrMnFeCoNi alloy after oxidation at 1000°C [24]. When one compares directly the oxygen mass gain obtained here for the CTR alloy only, to the 4.45 mg/cm$^2$ value, it seems that the CTR alloy presents a lower mass gain, taking into account that the oxidation duration in the present work was twice the one for the earlier results (2 to 3 mg/cm$^2$ here against 4.45 mg/cm$^2$, for 50 hours here against 24h). This may be a consequence of the differences in alloy synthesis procedure (vacuum induction casting in both cases, but followed by hot rolling followed by homogenization heat treatment in [24]), and thus in grain size for instance (here 1 – 2 mm against about 250 µm in [24]). The grain size is effectively of great importance at temperatures close to 1000°C and below, with more intensive intergrain diffusion predominating on volume diffusion when the oxidizing alloy is fine–grained.

The values of parabolic constants deduced here (Table 4 too) are spread out over a large interval ($13 \times 10^{-12}$ g$^2$ cm$^{-4}$ s$^{-1}$ to ten times this value). The Kp value obtained at 1000°C for the cast then hot rolled equimolar CrMnFeCoNi [24] was 0.83 mg$^2$ / cm$^4$ / h (i.e. $230 \times 10^{-12}$ g$^2$ cm$^{-4}$ s$^{-1}$), as is to say rather higher than the values obtained in the present work. One can again evocate the probable effect of the difference in microstructural fineness. By looking to the ranges of Kp values of the CTR, CTR+TaC and CTR+HfC alloys, one confirms that the presence of the Ta and Hf reactive elements, and of the corresponding carbides, are harmful for the oxidation resistance of the alloys. The deterioration in oxidation behavior is however rather low for the CTR+TaC alloy, by comparison with the CTR+HfC alloy.

## Conclusion

TaC and HfC are carbides that demonstrated efficient strengthening for the equimolar CoNiFeMnCr HEA alloy, as shown with recent high temperature creep tests in another study. But it appears that the presence of these carbides induces a more or less dramatic evolution of the oxidation behavior. Among the two types of carbides for reinforcement, only TaC allows high mechanical resistance at elevated temperature without threatening dangerously the oxidation resistance. This one is only a little decreased. Global high performance during high temperature service can be expected with the TaC–strengthened version of the equimolar CoNiFeMnCr HEA alloy.

## Data Availability statement

No data corresponding to this work is available.

## References

[1] P. Berthod, *J. Alloys Compd.* **2009**, *481*, 746.

[2] S. Michon, L. Aranda, P. Berthod, P. Steinmetz, Metall. Res. Technol. **2004**, 9, 651.

[3] P. Berthod, E. Conrath, *Mater. Des.* **2016**, *104*, 27.

[4] P. Berthod, E. Conrath, *J. Mater. Sci. Technol. Res.* **2014**, *1,* 7.

[5] A. Smekhova, A. Kuzmin, K. Siemensmeyer, R. Abrudan, U. Reinholz, A.G. Buzanich, M. Schneider, G. Laplanche, K.V. Yusenko, *J. Alloys Compd.* **2022**, 920, 165999.

[6] B. Cantor, *Prog. Mater. Sci.* **2021**, *120,* 100754.

[7] F.D.C. Garcia Filho, R.O. Ritchie, M.A. Meyers, S.N. Moteiro, *J. Mater. Res. Technol.* **2022**, *17,* 1868.

[8] W.M. Choi, S. Jung, Y.H. Jo,, S. Lee, B. J. Lee, *Met. Mater. Int.* **2017**, *23,* 829.

[9] G. Bracq, M. Laurent-Brocq, L. Perriere, R. pires, J.M. Joubert, I. Guillot, *Acta Mater.* **2017**, *128*, 327.

[10] S.F. Liu, Y. Wu, H.T. Wang, J.Y. He, J.B. Liu, C.X. Chen, X.J. Liu, H. Wang, Z.P. Lu, *Intermetallics* **2018**, *93*, 269.

[11] P. Berthod, *J. Met. Material Res.* **2022**, *5*, 1.

[12] P. Berthod, *J. Eng. Sci. Innov.* **2022**, *7,* 305.

[13] H. Song, Q. Ma, W. Zhang, F. Tian, *J. Alloys Compd.* **2021**, *885,* 160944.

[14] J. Sebesta, K. Carva, D. Legut, *Phys. Rev. B* **2021**, *103*, 064407.

[15] W. Kucza, J. Dabrowa, G. Cieslak, K. Berent, T. Kulik, M. Danielewski, *J. Alloys Compd.* **2018**, *731,* 920.

[16] C. Varvenne, A. Luque, W.A. Curtin, *Acta Mater.* **2016**, *118,* 164.

[17] Z. Zeng, M. Xiang, D. Zhang, J. Shi, W. Wang, X. Tang, W. Tang, Y. Wang, X. Ma, Z. Chen, et al, *J. Mater. Res. Technol.* **2021**, *15*, 1920.

[18] P. Berthod, *Proc. TMS 2023 San Diego* **2023**, accepted paper.

[19] M. Garg, H.S. Grewal, R.K. Sharma, H.S. Arora, *ACS Omega* **2022**, *7,* 12589.

[20] M.B. Venkataraman, A. Allanore, N. Birbilis, *NPJ Mater. Degrad.* **2020**, *4,* 25.

[21] L. Wang, Q. Zeng, Z. Xie, Y. Zhang, H. Gao, *Materials.* **2021**, *14,* 4259.

[22] S. Xia, C.M. Lousada, H. Mao, A.C. Maier, P.A. Korzhavyi, R. Sandström, Y. Wang, Y. Zhang, *Front. Mater. Sci.* **2018**, *5*, 53.

[23] G. Laplanche, U.F. Volkert, G. Eggeler, E.P. George, *Oxid. Met.* **2016**, *85,* 629.

[24] Y.K. Kim, Y.A. Joo, H.S. Kim, K.A. Lee, *Intermetallics* **2018**, *98,* 45.

[25] B.L. Pan, M. Wang, Y.G. Shen, X.L. Xi, Z.R. Nie, *China Foundry.* **2022**, *19*, 503.

# TABLES

Table 1. Chemical compositions of the three alloys

| **CTR<br>(Cantor alloy)** | **20 ± 0.5** | **21.5 ± 0.5** | **19.5 ± 0.5** | **19.5 ± 0.5** | **20 ± 0.5** | **N/A** |
|---|---|---|---|---|---|---|
| CTR + TaC<br>(including 0.25 Wt.% C) | 19.5 ± 0.5 | 20 ± 0.5 | 18.5 ± 0.5 | 18.5 ± 0.5 | 19 ± 0.5 | 4.5 ± 0.5<br>(M = Ta) |
| CTR + HfC<br>(including 0.25 Wt.% C) | 20 ± 0.5 | 20 ± 0.5 | 18.5 ± 0.5 | 18 ± 0.5 | 19.5 ± 0.5 | 4 ± 0.5<br>(M = Hf) |
| Weight contents: | Wt.% Co | Wt.% Ni | Wt.% Fe | Wt.% Mn | Wt.% Cr | Wt.% M |

Table 2. Results of exploitation of the concentration profiles to estimate some parameters characterizing the depletion in chromium and in manganese

| **CTR<br>(Cantor alloy)** | **7.5 – 10.5** | **2 – 2.5** | **53 – 64** | **64 – 92** |
|---|---|---|---|---|
| CTR + TaC<br>(including 0.25 Wt.% C) | 10.5 – 11 | 1.5 – 2 | 53 – 57 | 100 – 140 |
| CTR + HfC<br>(including 0.25 Wt.% C) | 5.5 – 13 | 1.5 – 2 | 46 – 64 | 100 – 110 |
| Depletion parameters: | Mini Wt.% Cr close oxid. front | Mini Wt.% Mn close oxid. front | Cr depletion depth (µm) | Mn depletion depth (µm) |

Table 3. Results of exploitation of the concentration profiles to estimate some parameters characterizing the depletion in chromium and in manganese; corresponding quantities of (Mn,Cr)3O4 oxide

| **CTR<br>(Cantor alloy)** | **1 – 2** | **4 – 5** | **7.7 – 10.2** | **16 – 21** |
|---|---|---|---|---|
| CTR + TaC<br>(including 0.25 Wt.% C) | 1 – 2 | 5 – 7 | 8.4 – 11.8 | 17 – 24 |
| CTR + HfC<br>(including 0.25 Wt.% C) | 1 – 3 | 7 – 9 | 10.6 – 11.4 | 22 – 49 |
| Depletion parameters: | Lost Cr ($mg/cm^2$) | Lost Mn ($mg/cm^2$) | Corresp$^{\underline{dng}}$ $(Mn,Cr)_3O_4$ mass ($mg/cm^2$) | Corresp$^{\underline{dng}}$ $(Mn,Cr)_3O_4$ thickness (µm) |

Table 4. Corresponding values of mass gains and of equivalent parabolic constants

| **CTR<br>(Cantor alloy)** | **2.2 – 2.9** | **13 – 23 ($\times 10^{-12}$)** |
|---|---|---|
| CTR + TaC<br>(including 0.25 Wt.% C) | 2.4 – 3.3 | 16 – 31 ($\times 10^{-12}$) |
| CTR + HfC<br>(including 0.25 Wt.% C) | 3.0 – 6.8 | 24 – 127 ($\times 10^{-12}$) |
| Depletion parameters: | Gained O ($mg/cm^2$) | Corresp$^{\underline{dng}}$ Kp ($g^2\ cm^{-4}\ s^{-1}$) |

# FIGURES

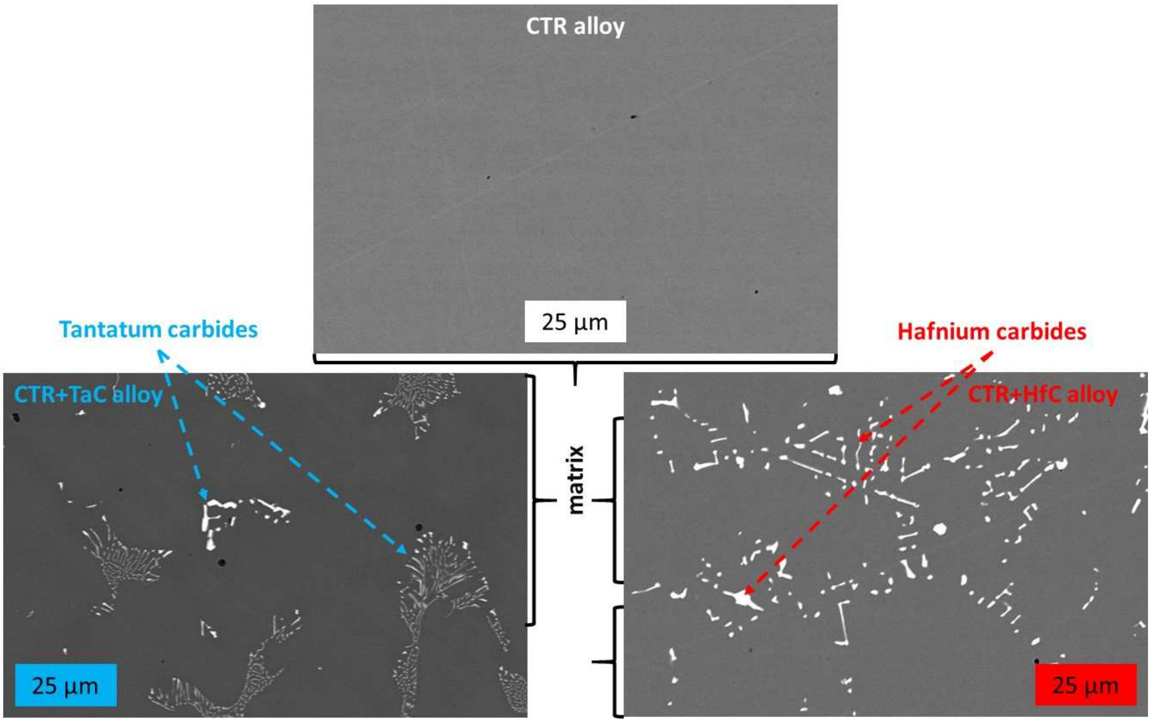

Figure 1. Microstructures of the three alloys in their as–cast states

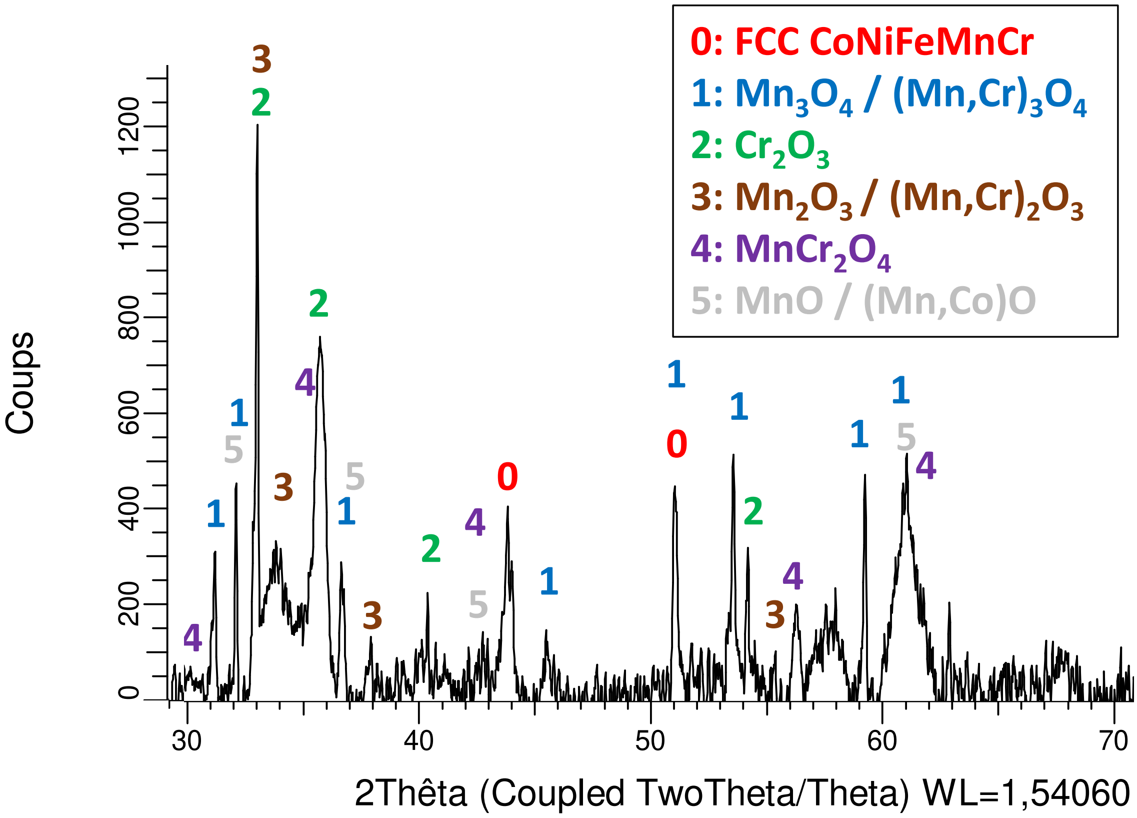

Figure 2. XRD pattern obtained on the oxidized surface of the CTR alloy

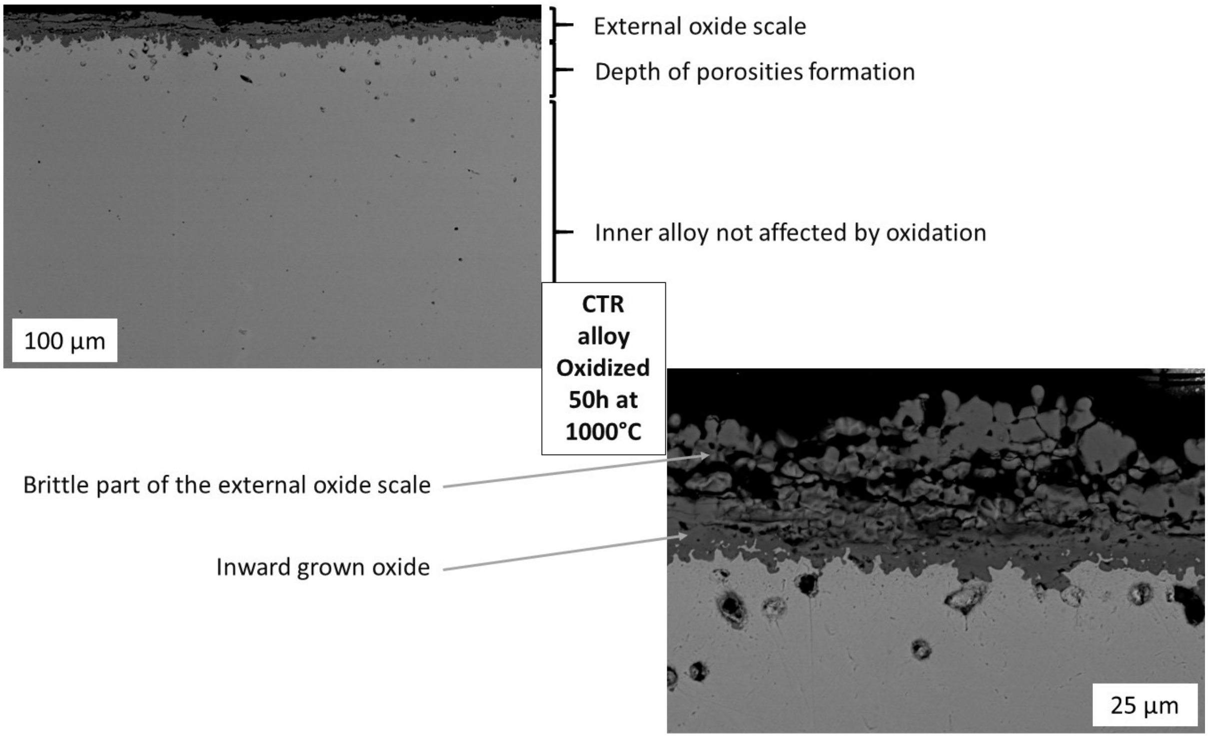

Figure 3. Low magnification and high magnification SEM/BSE micrographs illustrating the surface and subsurface deterioration of the CTR alloy

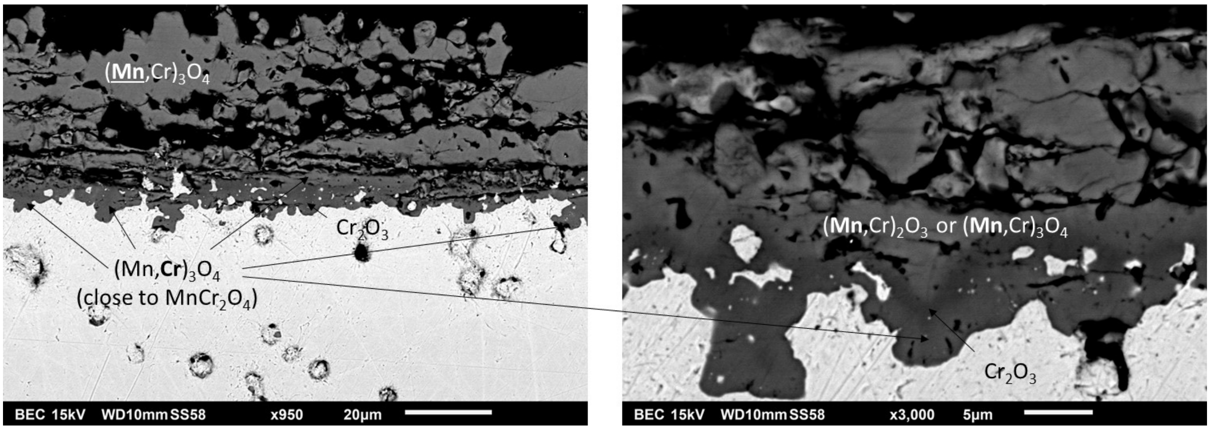

Figure 4. Additional high magnification pictures of the oxidized CTR surface and subsurface; identification of the different oxides using EDS spot analysis

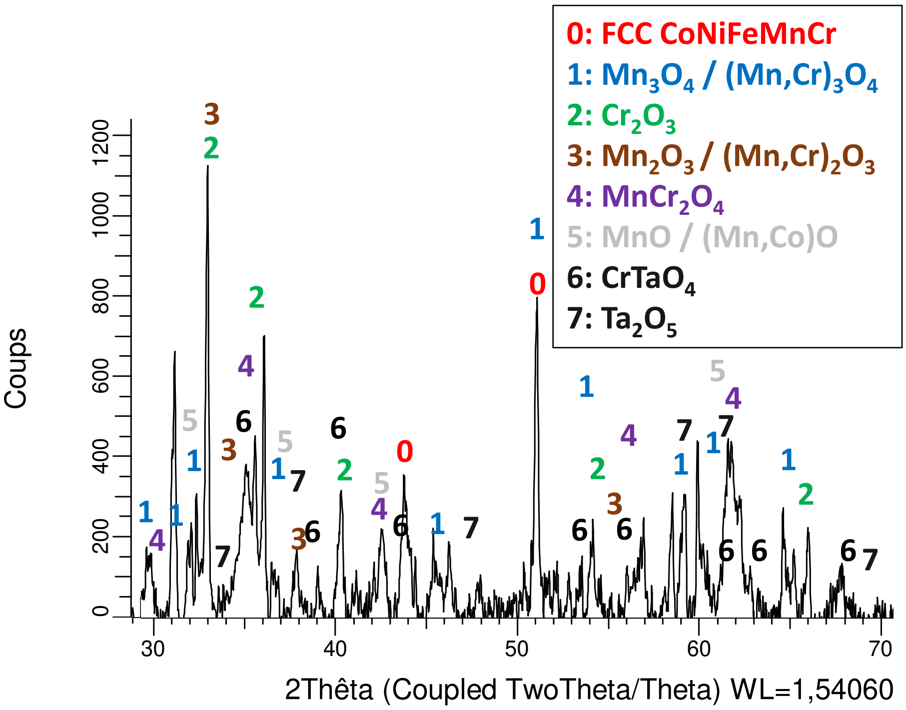

Figure 5. XRD pattern obtained on the oxidized surface of the CTR+TaC alloy

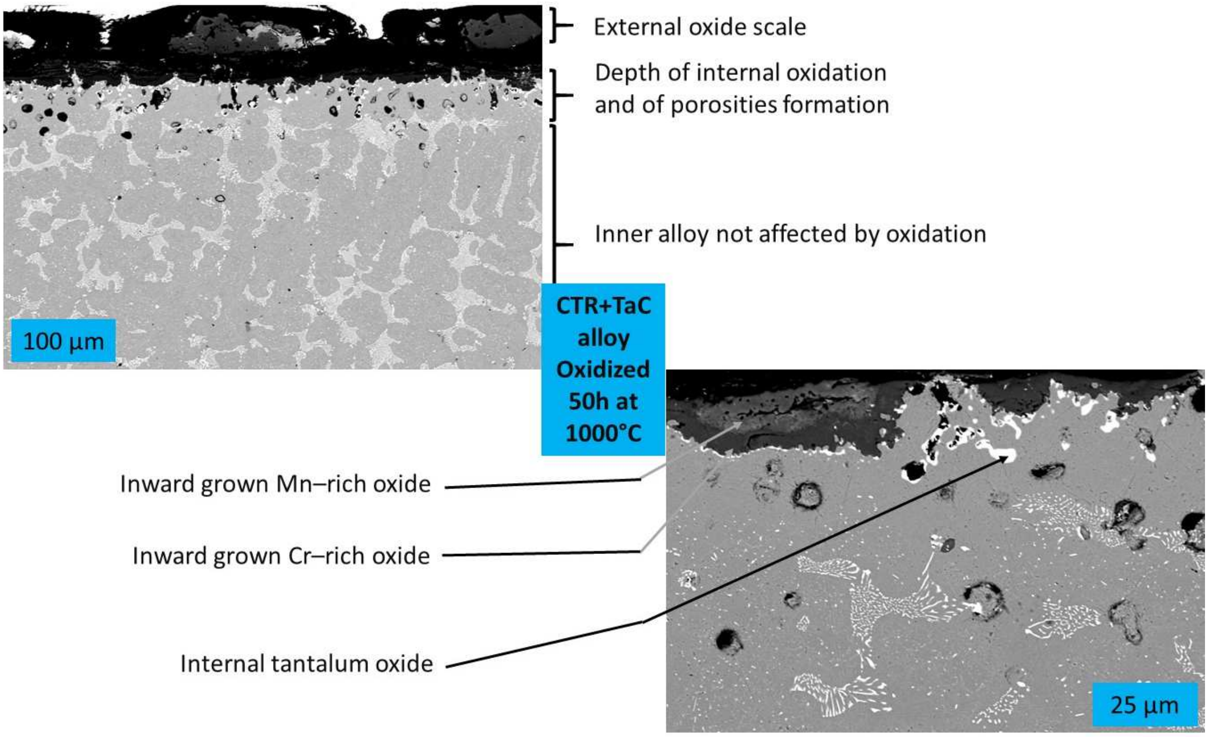

Figure 6. Low magnification and high magnification SEM/BSE micrographs illustrating the surface and subsurface deterioration of the CTR+TaC alloy

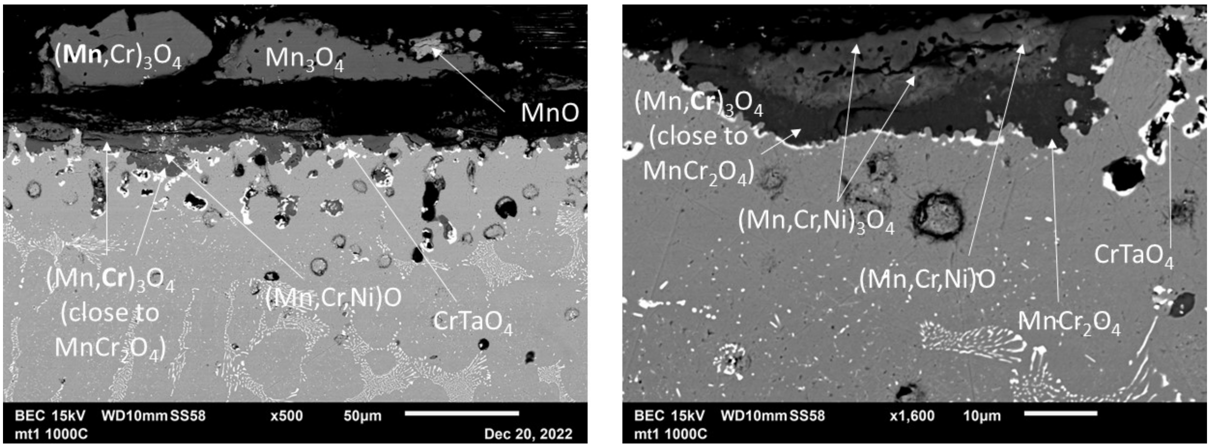

Figure 7. Additional high magnification pictures of the oxidized CTR+TaC surface and subsurface; identification of the different oxides using EDS spot analysis

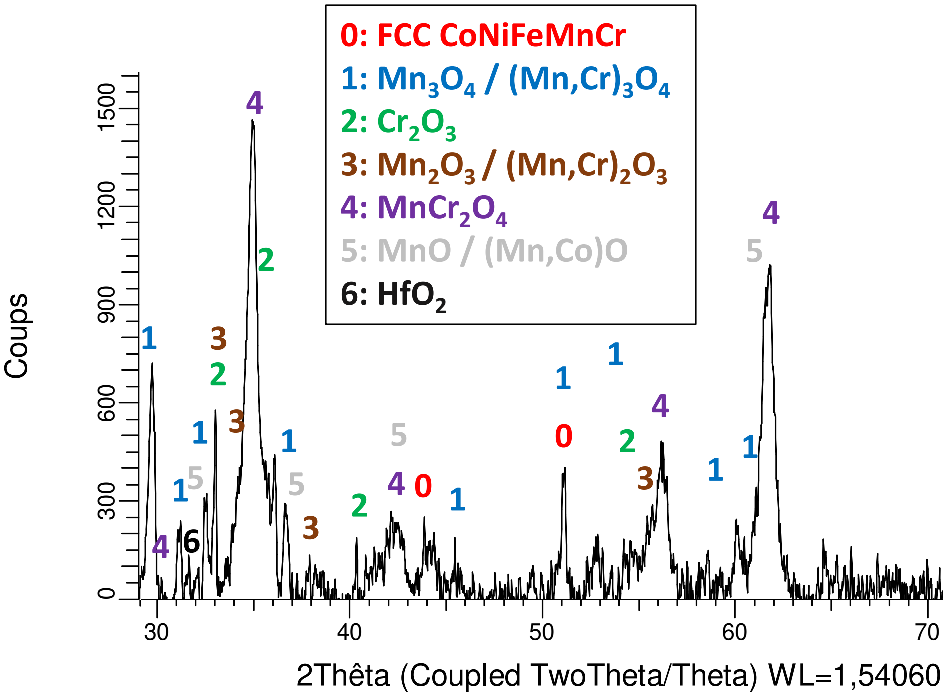

Figure 8. XRD pattern obtained on the oxidized surface of the CTR+HfC alloy

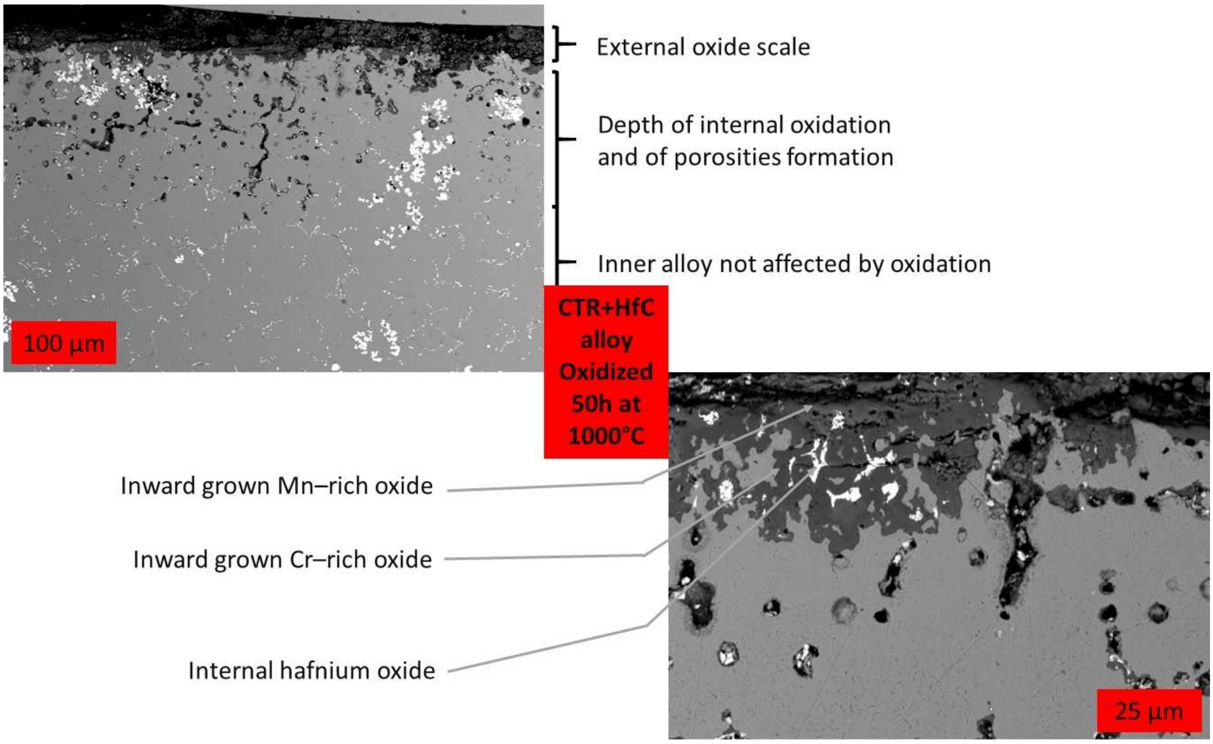

Figure 9. Low magnification and high magnification SEM/BSE micrographs illustrating the surface and subsurface deterioration of the CTR+HfC alloy

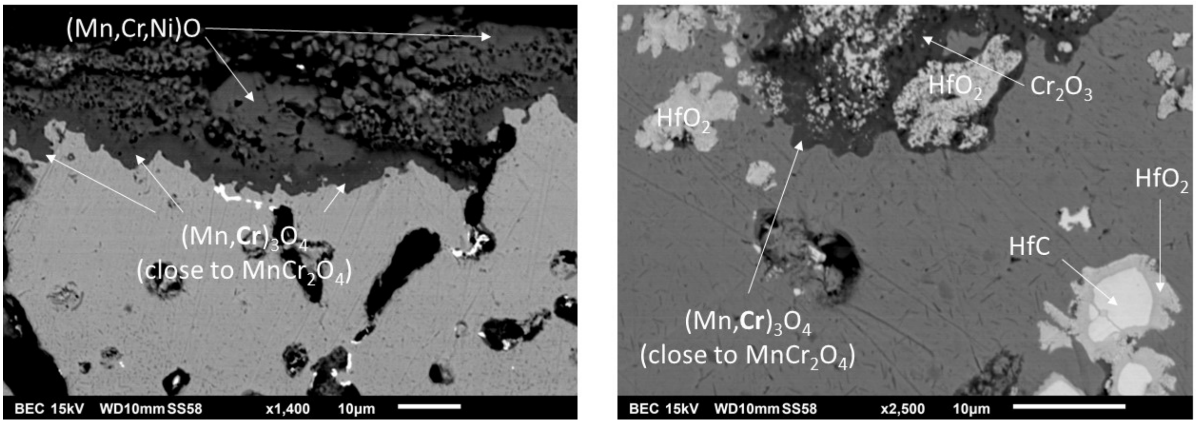

Figure 10. Additional high magnification pictures of the oxidized CTR+HfC surface and subsurface; identification of the different oxides using EDS spot analysis

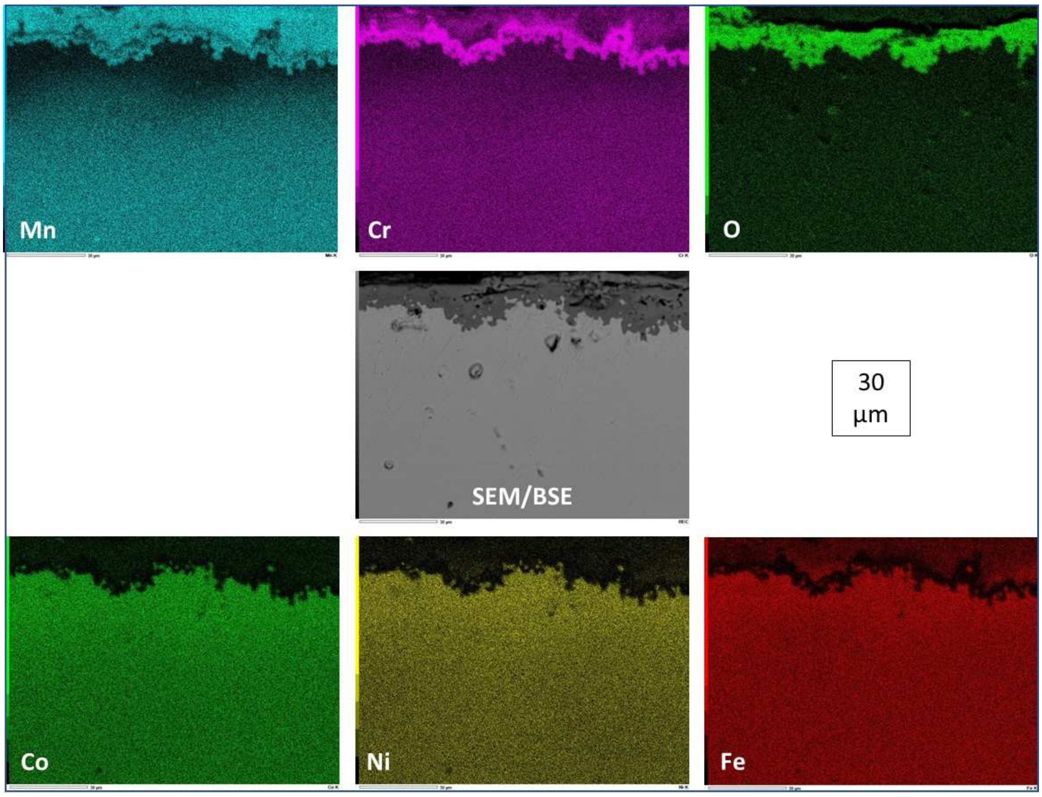

Figure 11. X–mapping of the oxidized surface and subsurface of the CTR alloy

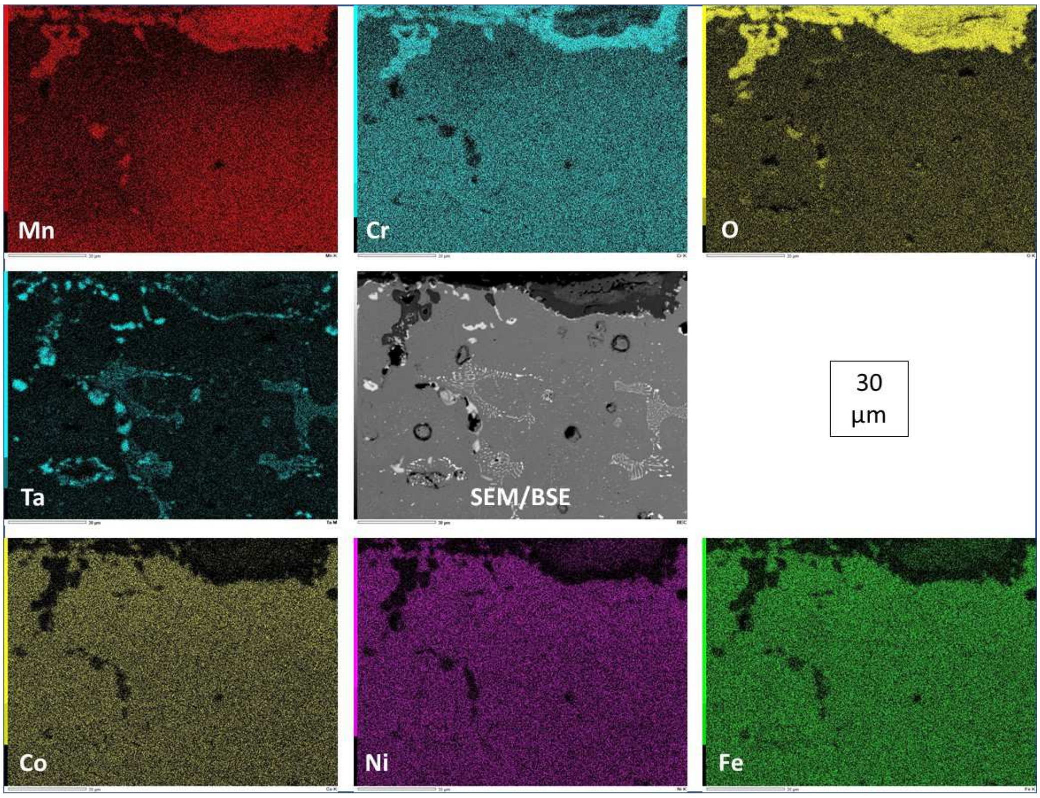

Figure 12. X–mapping of the oxidized surface and subsurface of the CTR+TaC alloy

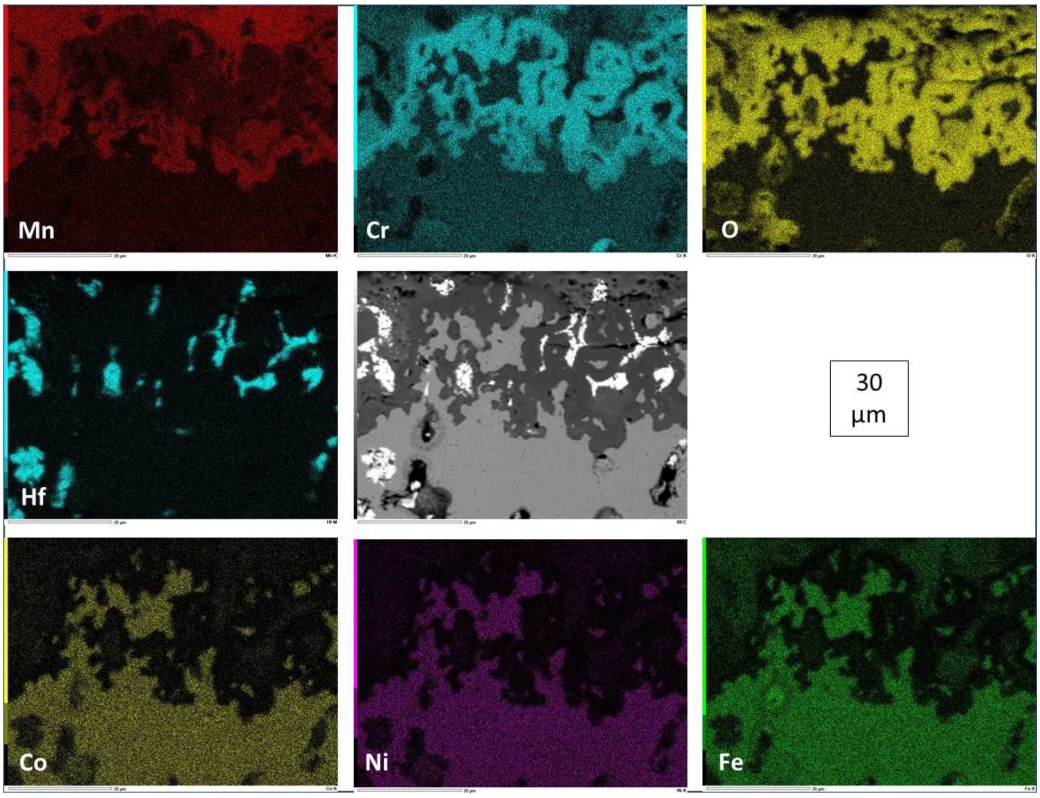

Figure 13. X–mapping of the oxidized surface and subsurface of the CTR+HfC alloy

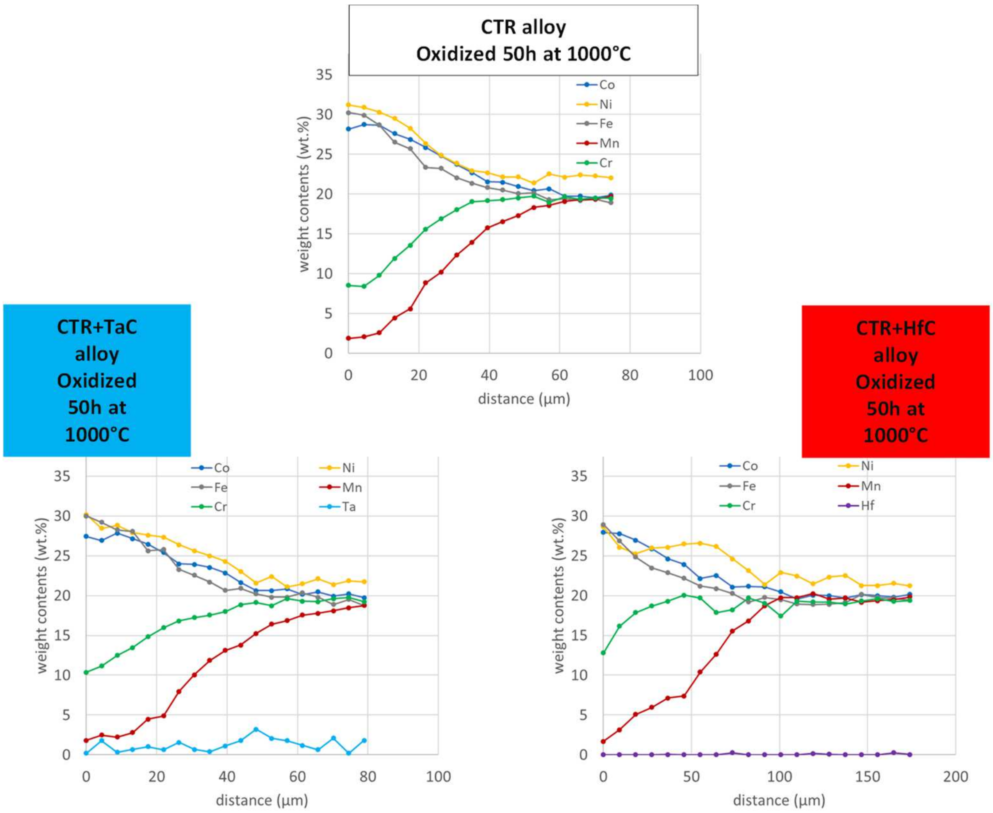

Figure 14. Examples of concentration profiles existing in the sub-surfaces of the three oxidized alloys (top: CTR alloy, bottom-left: CTR+TaC alloy, bottom-right: CTR+HfC alloy)